Full length article

4D synchrotron X-ray tomographic quantification of the transition from cellular to dendrite growth during directional solidification

B. Cai [a, b, **], J. Wang [a, b], A. Kao [c], K. Pericleous [c], A.B. Phillion [d], R.C. Atwood [e], P.D. Lee [a, b, *]

[a] School of Materials, The University of Manchester, Oxford Rd., M13 9PL, UK
[b] Research Complex at Harwell, Rutherford Appleton Laboratory, Harwell, Oxfordshire, OX11 0FA, UK
[c] Centre for Numerical Modelling and Process Analysis, University of Greenwich, Old Naval College, Park Row, London, SE10 9LS, UK
[d] Department of Materials Science and Engineering, McMaster University, 1280 Main St West, Hamilton, ONL8S 4L7, Canada
[e] Diamond Light Source Ltd., Harwell Science and Innovation Campus, Didcot, OX11 0DE, UK

ARTICLE INFO

ABSTRACT

Solidification morphology directly impacts the mechanical properties of materials; hence many models of the morphological evolution of dendritic structures have been formulated. However, there is a paucity of validation data for directional solidification models, especially the direct observations of metallic alloys, both for cellular and dendritic structures. In this study, we performed 4D synchrotron X-ray tomographic imaging (three spatial directions plus time), to study the transition from cellular to a columnar dendritic morphology and the subsequent growth of columnar dendrite in a temperature gradient stage. The cellular morphology was found to be highly complex, with frequent lateral bridging. Protrusions growing out of the cellular front with the onset of morphological instabilities were captured, together with the subsequent development of these protrusions into established dendrites. Other mechanisms affecting the solidification microstructure, including dendrite fragmentation/pinch-off were also captured and the quantitative results were compared to proposed mechanisms. The results demonstrate that 4D imaging can provide new data to both inform and validate solidification models.

© 2016 Acta Materialia Inc. Published by Elsevier Ltd. This is an open access article under the CC BY license (http://creativecommons.org/licenses/by/4.0/).

1. Introduction

Dendritic patterns formed during alloy solidification are the result of a complicated and dynamic process attracting significant scientific and practical interest [1—3]. Dendrites initially form because of morphological instabilities at the solid-liquid interface, and then grow rapidly because of a combination of effects related to solute partitioning between the solid and liquid and the thermal undercooling of the system. This process is influenced not only by the intrinsic properties of the alloy (e.g. the anisotropy of the solid/liquid surface energy and atom attachment kinetics), but also by extrinsic conditions (e.g. fluid flow which can be induced by buoyancy, or driven by magnetic fields) [1,4]. One approach to obtaining dendrites in a controlled manner is by directional solidification (DS). DS is used industrially in metallic alloy systems to create components with a specified columnar microstructure, strongly enhancing the performance of materials. For example, columnar/single crystal Ni-based superalloys used for turbine blades are manufactured by DS methods with improved mechanical properties [5]. The dendrite pattern is important in several other natural and applied fields, ranging from hydrodynamics and chemistry to biology [6—8]. The DS technique can also be used in these fields to examine pattern formation mechanisms [9,10].

Research in the field of DS has resulted in a number of analytical solutions [1,11] and numerical models [12—14] to predict the development of the microstructure. However, accurate prediction of dendritic patterns is still difficult since these solidification models contain mathematical simplifications and physical parameters, both of which are often experimentally calibrated. Hence, validation by targeted experiments is critical for their further development. One popular approach is to resolve the dendritic morphology in situ via transparent organic alloys coupled with optical imaging [15,16] and/or metallic alloys with X-ray radiography [17—20]. DS is then achieved using temperature gradient furnaces [21—24], illuminating many aspects of solidification science, including interface instabilities [25,26], columnar dendrite

growth [27,28] and dendrite fragmentation [29,30]. Transparent organics have been extensively used due to not only their morphological similarity to metallic alloys but also their low melting points [15]. For direct imaging of metallic dendrites, high speed X-ray radiography must be performed using very thin metallic samples (100—200 μm) [22,28,31—33]. While these techniques have thus far provided the basis of our understanding of dendritic solidification, both optical imaging and X-ray radiography are inherently 2D, thus morphological changes on the surface perpendicular to the incoming beam cannot be captured. Further, the usage of thin samples restricts the growth of the solid phase, and hence may not be representative of the bulk sample.

The recent development of high speed synchrotron tomography allows for *in situ* imaging of relatively bulky samples during solidification experimentation, enabling so-called 4D X-ray imaging (*x*, *y*, *z* plus time) of microstructure evolution. This technique has been applied to study solidification problems with great success, including equiaxed dendrite morphology evolution [34—36], solid phase coarsening [37], and semi-solid deformation [38—40]. However, to date, experimental designs enabling 4D imaging of directional solidification remain unexplored. In this study, the application of a temperature gradient stage integrated with high speed synchrotron X-ray tomography to study columnar dendrite growth of an Al—Cu alloy during directional solidification is reported. This time-resolved tomographic imaging has enabled 4D observation and quantitation of key solidification phenomena: cellular growth, interface insterbilities and the transition to columnar dendritic growth, together with dendrite fragmentation, which were previously only accessible via *in situ* 2D methods. The findings are of interest to not only microstructural engineering of advanced metallic alloys, but also to the broader field of pattern formation and crystal growth, providing a unique dataset for model validation.

2. Experimental methods

2.1. Materials and furnace design

A bespoke temperature gradient stage incorporating two furnaces (the upper furnace reaching 1000 °C, the lower 600 °C) was designed and commissioned allowing combined tomography and directional solidification (Fig. 1). The upper furnace utilizes a heating element made from 1 mm diameter Ni—Cr alloy wire (Omega Engineering Limited, UK) coiled to an alumina tube with an inner diameter (ID) of 10 mm and outer diameter (OD) of 17 mm. The lower furnace utilizes a heating element made from four cartridge heaters inserted into a Cu block with a central hole of 10 mm

diameter. The two furnaces were aligned so that the two 10 mm central holes were in parallel, having a 12 mm gap for the X-ray beam, covered with thermal insulation.

An Al-15 wt%Cu alloy was selected for this study. This alloy has a high absorption contrast between Cu-enriched liquid and the solid, facilitating observation of dendrite patterns via X-ray tomography. For the experiment, a sample 3 mm in diameter and 100 mm in length was inserted into an alumina tube (ID 3 mm, OD 5 mm). The tube and the sample were then mounted on the top of a Cu sample holder. This assembly was then mounted onto a goniometer and centreed within the middle of the temperature gradient stage to allow for directional solidification.

2.2. Synchrotron tomography measurement

High-speed absorption-based X-ray tomography was performed on the I12 beamline at the Diamond Light Source using a 53 keV monochromatic X-ray beam (wavelength 0.023 nm). To acquire the X-ray radiographs, a PCO.edge camera was coupled with I12's camera module 3 [41], offering a field of view (FOV) of 2560×2160 pixels, and a pixel size of 3.9 μm. The FOV was further cropped to 1070×1070 pixels, corresponding to 4173×4173 μm to increase acquisition speed. One tomogram consisted of 900 projections over 180° with an exposure time of 5 ms per projection, hence the total time per tomogram was 4.5 s. After inclusion of additional sample rotation and data download, the cycle time was 9 s. These conditions allowed continuous visualisation of the dendrite growth of a 3 mm diameter Al—Cu sample during solidification using a relatively large FOV.

After placing the sample holder within the furnace and aligning with the X-ray detector, the experiment was conducted as follows. First, both furnaces were heated until melting was visible in the FOV. Then, the temperatures of both furnaces were adjusted to ensure the presence of a stable solid/liquid interface at the bottom of FOV. Note that it was necessary to re-melt the sample several times to achieve this stable interface. At the start of solidification, the temperature of the sample just under the top furnace was 637 °C and just above the bottom furnace was 510 °C, measured by a K-type thermocouple. This corresponded to an initial thermal gradient of ~11 °C/mm. This thermal condition was maintained for 10 min. Then, the temperature of the bottom furnace was lowered at a rate of about 0.27 °C/s, known as power down method [42], while the temperature of the top furnace was maintained, to achieve solidification within the FOV. This method results in an increase in the thermal gradient over time, which could not be directly measured as attaching thermocouples onto the sample is challenging due to sample rotation. X-ray tomographic imaging was initiated when the cooling down started. Overall, 50 tomograms were collected during the solidification process, spanning 441 s.

2.3. Image quantification

A filtered back-projection algorithm was used to perform the reconstruction with a ring removal method [42]. 3D image quantification techniques, implemented in Avizo 8 (FEI VSG, France) (application of an anisotropic diffusion filter, and global thresholding of the pore, solid, and liquid phases using the Otsu method [43]), were used to further improve the image quality and thus to observe the directional solidification. Afterwards, various quantifications were performed on the enhanced images, including (1) calculation of the solid fraction (f_s) within the field of view, (2) determination of the local diameter (termed local thickness) of the cellular structures using BoneJ [44], which measures the diameter of a biggest sphere that can fit into the 3D structure, and (3)
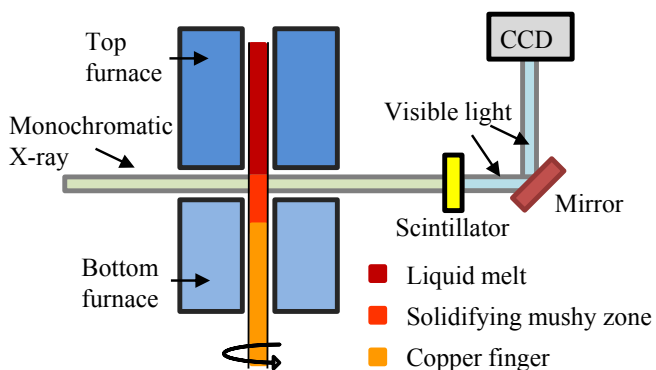

Fig. 1. Schematic of the temperature gradient furnace for high speed X-ray tomography.

dendrite curvature. To study dendrite growth, a single dendrite was selected through a semi-automatic method from the complex dendritic assembly. For this segmentation, an image mask covering a single dendrite was created from the final tomography through careful visual observations. Then, the mask was first applied back to all tomograms, and the dendrite was segmented from the masked region.

3. Results and discussion

General observations of microstructural development during the cooling down are presented first, followed by detailed quantification of the different stages of solidification, including cellular growth and coarsening, cellular to dendritic transition, and dendritic growth and fragmentation.

3.1. Overall observations

Fig. 2a—e shows 2D vertical slices extracted from the centre of the X-ray tomographic datasets at progressive solidification times of the Al-15 wt.%Cu alloy ($t = 0$, 180, 225, 279, and 441 s). Through these images, a qualitative description of the solidification process can be obtained. In the first image (Fig. 2a) corresponding to the initial solidification within the FOV, a few cellular solid structures can be observed. The initial 3D solid microstructure, shown as the yellow surface in Fig. 2a insert, also indicates a cellular structure. Note that these cells are probably growing epitaxially from the repeatedly re-melted structure formed while achieving an appropriate cooling rate and thermal gradient. Because of this, the cellular structure will be evolving, rather than established such as that formed during Bridgeman solidification. The red colour in this inset identifies an irregular-shaped pore that is connected to the sample surface. This pore was likely to have been shrinkage porosity kept in the melt via an entrained, surface connected, oxide.

The cells shown in Fig. 2a continue to grow upwards (Fig. 2b) as the bottom furnace was cooled. A cellular to dendritic transition then occurs, with fine dendritic structures forming (Figs. 2c and d) from the cellular phase. These dendrites quickly start branching, with secondary and tertiary arms forming. On the right-hand side, the cross-section of a few columnar grains can be observed that appear equiaxed-like. These dendrites tended to grow along the wall of the alumina tube. The dendrites continue to grow upwards as the sample cooling, forming complex branching patterns (Fig. 2d—e), with one particularly well-developed columnar dendrite on the left-hand side. The sequence for the microstructural development is hence as follows: the growth of initial cellular solid phase; the transition from cellular to dendritic structure; and subsequently growth of the newly-formed columnar dendrites.

Fig. 2f shows a transverse slice of the final tomography at $t = 441$ s (at the position marked by the red line in Fig. 2e). In total, 29 columnar dendrites can be seen in this slice, some with well-developed secondary and tertiary dendrite arms. Four-fold symmetry was observed consistently between the primary and secondary arms as expected in an FCC metal. Some of the tertiary arms, denoted by red arrows, were inclined at an angle of approx. 60° to the secondary arms, indicating possible deviation from crystallographic symmetry.

Fig. 3 provides a three dimensional rendering of the final tomographic image ($t = 441$ s) recorded during the DS experiment, rendered with a grey scale matching previously-published X-ray radiographic images [17,45]. This image shows that the DS grain morphology achieved is similar to prior results obtained via X-ray radiography [17], with columnar dendrites growing out of the cellular structure, and the formation of porosity [46]. As can be seen, the solid/liquid interface indicated by the curved purple line is quite uneven. This is due to complex convection in the melt, potentially induced by: (a) solute induced buoyancy driven flow [47], (b) radial inhomogeneous temperature gradient, and (c) the
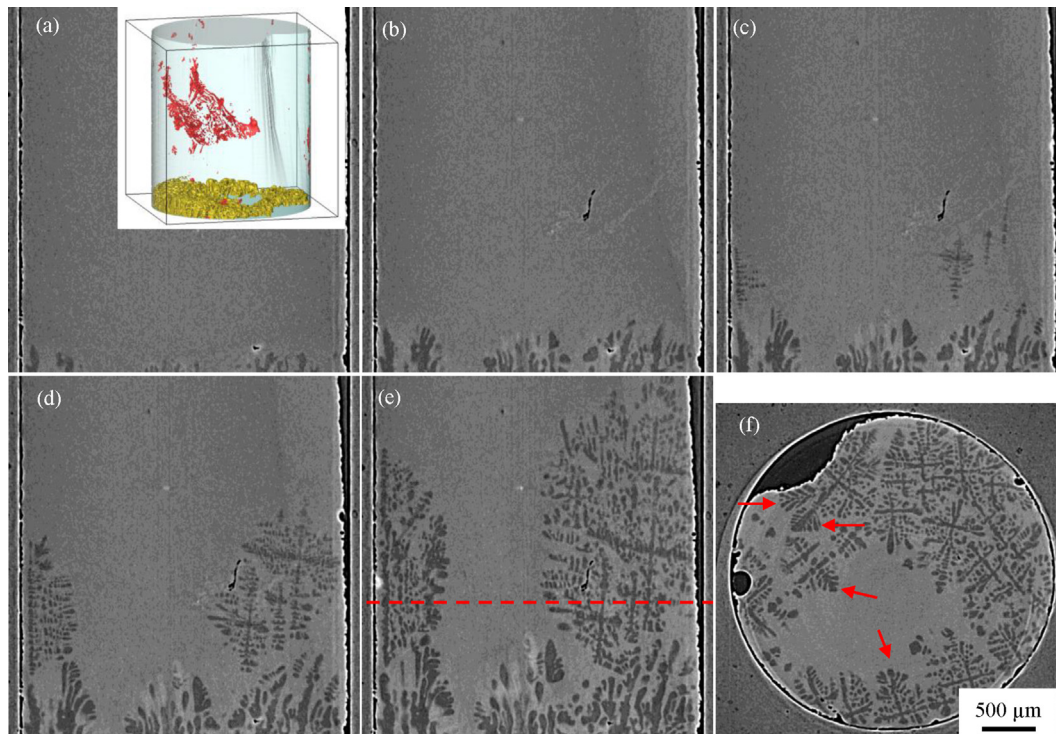

Fig. 2. (a to e) Longitudinal cross-sectioned slices extracted from tomographic volumes at $t = 0$, 180, 225 and 441 s, respectively; (f) transverse slice at the height of 1.29 mm from the bottom at $t = 441$ s. Insert in (a): porosity distribution (red) and initial solid phase (yellow) within the sample at $t = 0$ s (the transparent surface shows the shape of the sample).
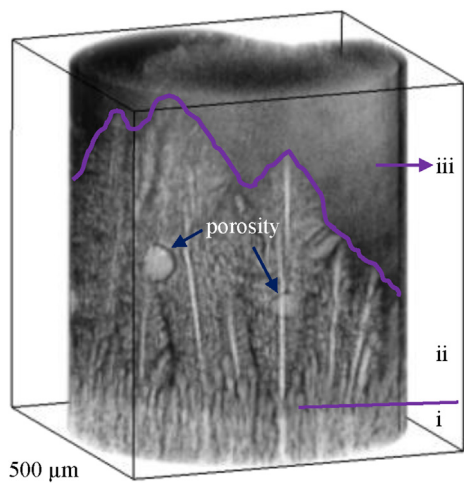
Fig. 3. Volume rendering of the final recorded tomography at $t = 441$ s after solidification was initiated.

rotation of the sample for tomographic imaging. From the dataset provided in Fig. 3, three distinct regions of grain morphology can be identified. The first, region (i), consists of a mainly cellular structure. The second, region (ii), has a dendritic structure. The third, region (iii), is liquid enriched with Cu rejected by the solidification front.

3.2. Cellular to dendritic transition

Figs. 4a, b and 4e show the 3D morphology of the evolving solid cellular structure at the bottom of the field of view (Region (i) in Fig.3), in which each cell has been coloured by its local thickness (T) and the liquid has been removed. The local thickness is calculated as the diameter of the biggest sphere that can fit into an individual cell. The initial solid growing from the bottom appears to be an established cellular structure (Fig. 4a) with a slightly uneven front. Zoomed views of the cellular structure at the same time points are shown in Figs. 4c and d (see also the supplementary video 1). The cellular structure develops over the first 180 s (Fig. 4b), at which point there is a sudden transition (around 153 s) to dendritic growth over most of the front. It is likely that the initial cellular structure (in Fig. 4a and those below the field of view) nucleated via epitaxy on the un-remelted solid below the field of view. Even at the early stages of this epitaxial cellular growth, the structures are very complex with undulating structures and lateral interconnectivity. This microstructure is much more complex than that visualised in thin organic analogues grown by the Bridgeman method [49]. Bergeon et al. [50] demonstrated that a similar cellular structure could form in a bulk transparent samples when viewed in a direction perpendicular to the solidification gradient. In the present experiments, the tremendous complexity related to the initial growing structure may also have been the result of re-melting of the sample in a temperature gradient leading to temperature gradient zone melting [51] and continuous microstructure coarsening.

Supplementary video related to this article can be found at http://dx.doi.org/10.1016/j.actamat.2016.07.002.

Fig. 4d (also see supplementary video 1) demonstrates that the cellular growth front becomes unstable across the whole field of view at approximately the same time (153 s) as they reach a Mullins-Sekerka morphological instability [11]. The perturbations in the front quickly form stable protrusions, capturing the first stage of the transition from cellular to dendritic growth in 4D for

the first time. The supplementary video tracks how these perturbations, formed of parabolic tips with cylindrical primary arms behind them transform into columnar dendrites, capturing the next stage of the transformation.

The cellular structures thicken both during early stages of growth, and later after the solid/liquid front is well past, as thermodynamics dictates more solid form. The evolution in local cell thickness is shown via the colouring in Fig. 4, both during cellular growth (Figs. 4a and b) and during the later stages of solidification (Fig. 4e) when the front is long past the field of view (FOV). The solid fraction (f_s) within the region shown in Fig. 4 (Region (i) in Fig. 3), was quantified as a function of the solidification time and is shown in Fig. 4f, along with the average solidification rate:

$$\dot{f}_s = \frac{f_s(i) - f_s(0)}{t(i)}, \ i = 0, \ 1, \ 2, \ ..., \ 49 \tag{1}$$

where $\dot{f}_s$ is the solidification rate, $f_s(i)$ is the relative solid fraction of Region (i) of ith tomography dataset ($i = 0,1, 2, ..., 49$), $f_s(0)$ is the relative solid fraction of Region (i) in the initial tomography dataset shown in Figs. 4a and $t(i)$ is the time at which the ith tomography dataset was acquired relative to the initial tomography dataset.

As can be seen in Fig. 4d, the fraction solid, f_s, increased from 15.1% to 46.7% but nonlinearly. The f_s initially increases slowly as a few cells entre the region, accelerating as the whole front moves through, and slowing at the end as cooling slows and the eutectic composition is approached. The solidification rate can be seen to rise almost linearly at the beginning, but above a threshold time, it slows (Fig. 4d). This threshold time (t_0+190 s) corresponded well with the time point when the growth mode within the FOV changed from cellular to dendritic. The transition-to, and growth of, dendrites will be analysed in the next sections.

3.3. Initial stage of dendritic growth

During alloy solidification, Mullins-Sekerka [11] instabilities form at the solid/liquid interface, with the rejection of solute favouring as large a solid/liquid interface as possible [48]. After the onset of the cellular to dendritic transition, a number of further interface instabilities were observed, including sidewise instabilities and tip-splitting, giving rise to dendritic and coral-like structures, respectively. Figs. 5a and b show the morphological evolution of the solid phase from 153 to 198 s (see supplementary video 2), the period during which such instabilities develop. The images represent a sub-volume 780 × 780 × 780 μm in size and taken from Region (ii) of Fig. 3. The solid phase is coloured by its mean curvature (note, a positive mean curvature means concave towards the liquid). As can be seen in Fig. 5a, the solid structure at 153 s starts as nearly cellular, with small perturbations with high curvatures forming (shown via arrows and shaded in red) that become dendrites. Within this region of interest, the cells grew upwards and expanded, as expected (see supplementary video 3). By 193 s, Fig. 5b, severe protrusions and side branches have developed. Note that although most cells have converted to dendrites, only a small portion in this region developed branches as the spacing is smaller than optimal, and many are overgrown. Of the branches formed, some were symmetric, obeying four-fold symmetry, while others were asymmetric.

Supplementary video related to this article can be found at http://dx.doi.org/10.1016/j.actamat.2016.07.002.

Fig. 5c–g show an example of an individual cell transitioning to a dendrite with four-fold morphology. Note that this dendrite was not located within the ROI shown in Fig. 5a. As can be seen, the initial cell is small and plate-like with a relatively smooth surface. The cap is flat and two small protrusions were found on the two
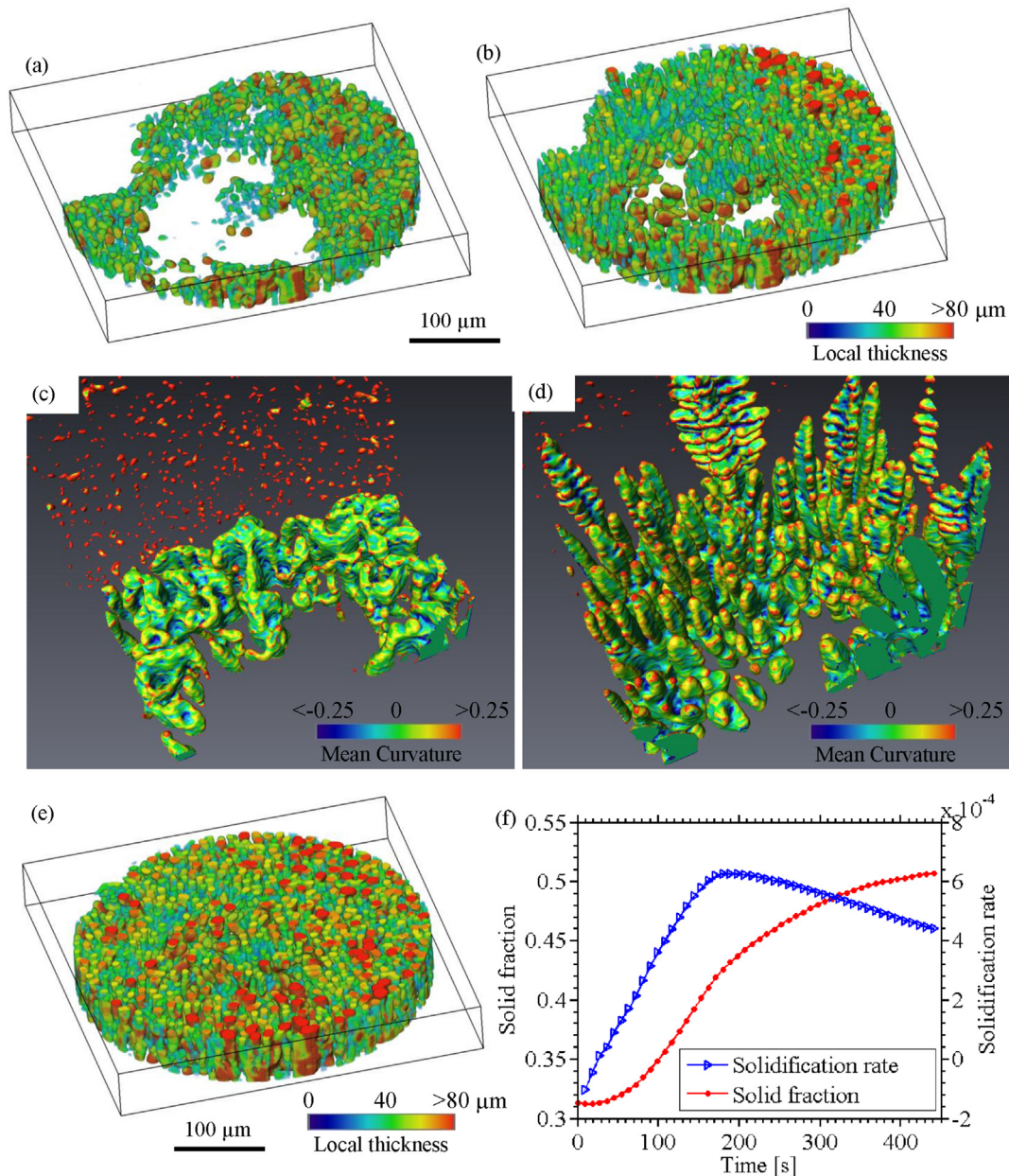
Fig. 4. (a) (b) and (e) Growth and coarsening of cellular structure at the bottom region of the field of view at $t = 0$, 180, and 441 s, respectively; (c) and (d) an enlarged view of the cellular structure at $t = 0$ and 180 s; (f) solid fraction and solidification rate as a function of solidification time.

corners of the cap. Fig. 5d shows that the tip of the cell split into two and also its root narrowed, possibly via local remelting. The right-hand tip grew upward, forming a primary arm. Side-branching perturbations then formed, perpendicular to the primary arm, which seem to have a parabolic tip shape, Fig. 5e. As solidification advances, the primary arm continues to grow, forming more side-branches from the perturbations (Figs. 5f and g), thus capturing 4D secondary arm formation. This dendrite out-grew the other two that sited on its left and right hand side. Four-fold symmetry is expected for the dendrite growth of this FCC alloy when growing along <001> direction, and nicely demonstrated by the secondary arms in Fig. 5g.

Distinct from classical four-fold symmetric growth, another type of interface instability, leading to asymmetric patterns was observed during the experiment (see Fig. 5h to l). The initial cell is shown in Fig. 5h. As can be seen, the thin cell has a flattened cap

with a small groove in its centre. Unlike the classic dendritic case, this cell expanded forming several principle protrusions, which are marked by black arrows in Fig.5h–j, creating a corrugated surface with large differences in curvature (Fig. 5j to l) and no obvious four-fold symmetry as shown in Fig. 5g. There are side-branches growing perpendicular to the principle stems, Figs. 5k and l. The resulting structure is a dense-branched 3D coralline-like morphology. The morphology observed here is similar to seaweed patterns. Seaweed microstructure has been observed in thin crystals imaged via 2D methods (both in thin transparent organics [49–51] and metallic alloys [52]). Several factors could be the origin of the seaweed pattern. Crystalline anisotropy can have a significant effect on the morphology of the solid-liquid interface. In this experiment, the crystalline anisotropy could stem from two potential sources. First, the sample was melted/re-solidified many times to achieve DS growth, forming the initial cellular structure.
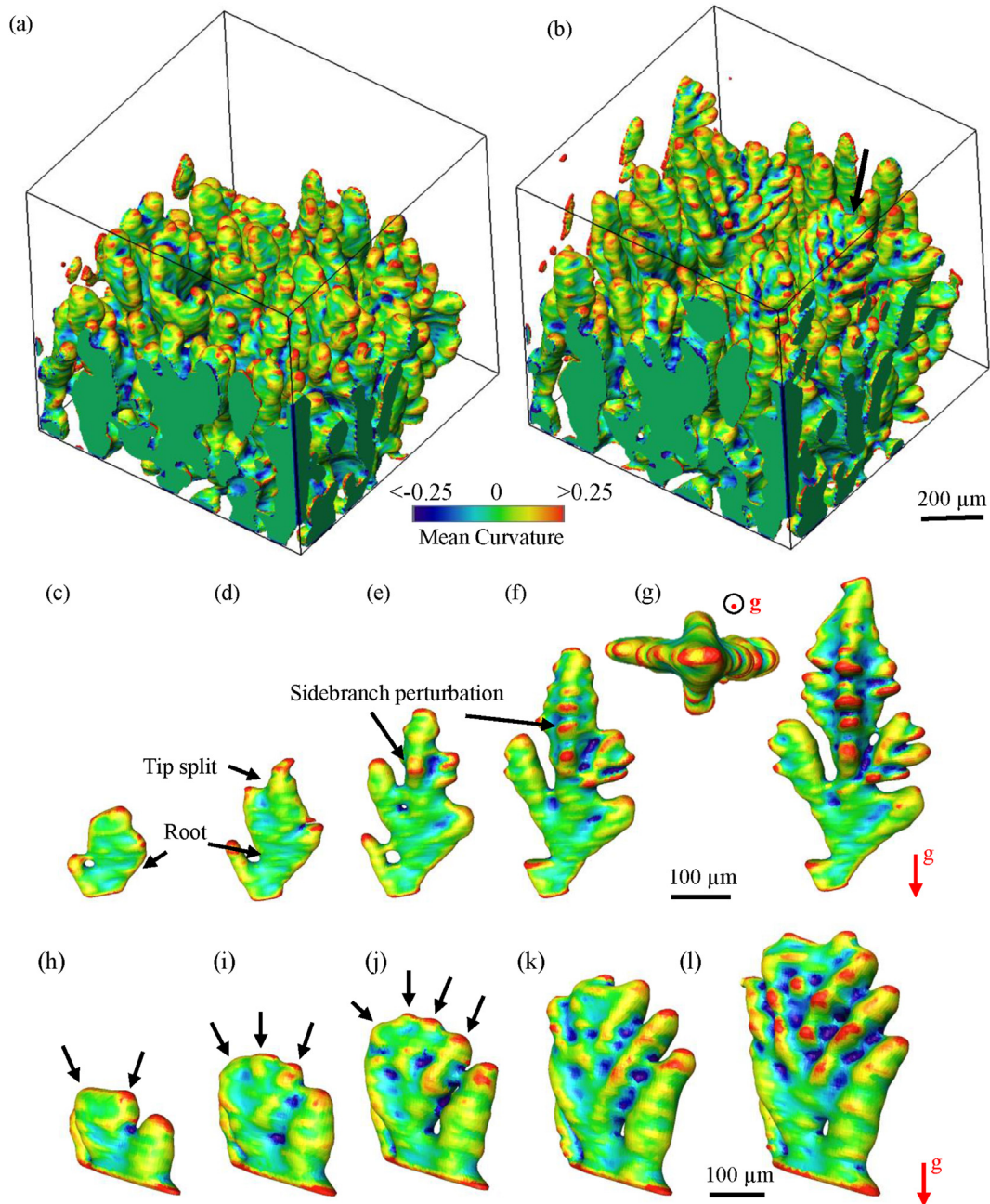
Fig. 5. (a to b) 3D interface morphology evolution coloured by its mean curvature at t = 153, and 198 s, respectively; Initial growth of (c to g) dendritic structure and (h to l) coralline-like morphology: (h) t = 153s; (c) and (i) t = 162 s; (d) and (j) t = 171 s; (e) and (k) t = 180 s; (f) and (l) t = 189 s; (g) t = 198 s.

Crystal growth orientation other than <001> could align to the upward thermal gradient. Second, those cells growing at <001> direction might be misoriented from the thermal gradient, which can also induce seaweed structure. Both have been experimentally observed in transparent model systems [54]. Unfortunately, in this case, EBSD could not be performed as the sample was subsequently re-melted.

3.4. Established dendrite growth

Well after the transition from cellular to dendritic structure, competitive growth of the dendrites occurs and the surviving ones become classical tree like structures. Established dendritic growth is shown in Fig. 6 for three solidification times (see also

supplementary movie 3) of a single dendrite (marked SD). Note it is the same dendrite as in Fig. 5c—g, picked as it is near the centre of the sample and is not constrained by the walls. As can be seen, this dendrite competed with neighbouring dendrites (red arrows, Fig. 6a) and outgrew them. It is well known that Al dendrites whose <100> preferential growth direction is almost parallel to the heat flow direction can grow very quickly, impeding less well aligned dendrites [53]. Thus it is probable that SD had preferred orientation in comparison to its neighbours. The blockage of the surrounding dendrites by the side branches of SD is clearly visible by comparing the sequence Fig. 6a-b-c-d. As can be seen, the nearby dendrites continuously deviated from SD, making space for its secondary arms to develop. In addition, the surfaces of the nearby dendrites facing SD are smooth without any secondary arms. This
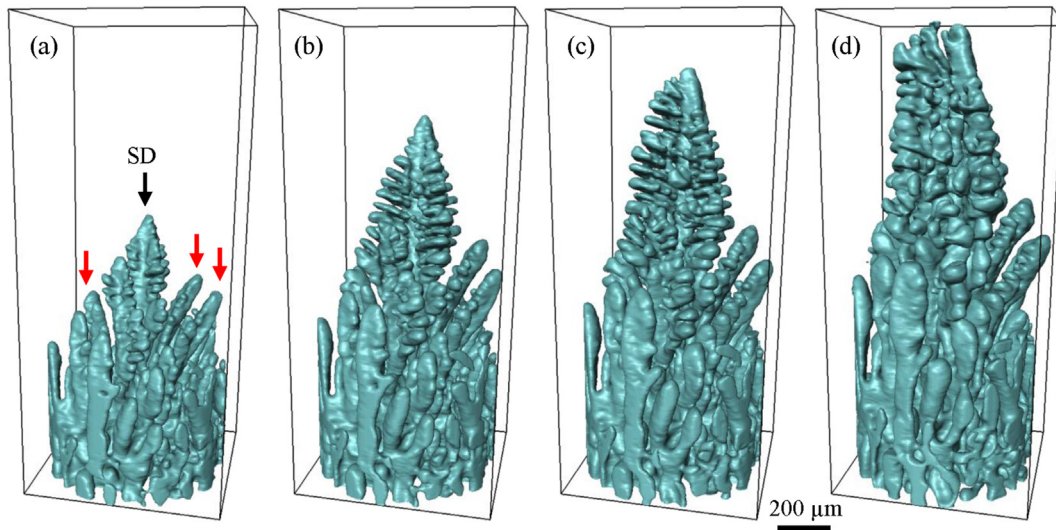
Fig. 6. (a to d) 3D morphology of dendrite structure at $t = 207$, 261, 306, and 441 s, respectively.

demonstrates the extent to which the side branches of SD caused these neighbour dendrites to incline away from the SD, and become growth inhibited. Finally, the shape of secondary arms was flat on the cold side but bulged on the hot side (close to the primary dendrite tip), unlike cylindrical [54] and plate-like [34] shape observed by others. These secondary arms were self-similar, and some merged together and ripened at later stages of solidification.

The instantaneous tip velocity of SD together with the tallest/foremost dendrite visible in Fig. 3, denoted as FD, is plotted in Fig. 7. Note: FD (close to the Alumna tube), may have grown faster/taller because of a combination of compositional heterogeneity due to sample remelting, as well as minor temperature variations. As can be seen in Fig. 7, the trends are the same, showing three different growth stages: (1) cellular growth with a slowly increasing velocity as the temperature and gradient decrease (0–150 s); (2) rapidly increasing growth rates immediately after the cellular structure breaks down into dendrite, which shoot off quickly (150–200 s); and (3) the slowdown of dendritic growth due to the cooling rate decreasing (>200 s). This data can be used to validate models of dendritic growth. Chen et al. [52] carried out an *in situ* radiographic observation of thin Al-4wt.%Cu solidified directionally using similar
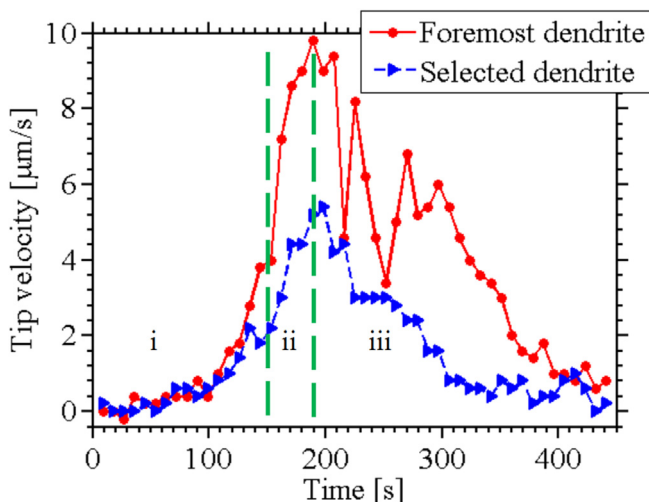
power down method. The velocity of the furthest tip of their study shows a similar trend. Although the 'power down' method leads to a continuous increase in the temperature gradient along the sample, this increase may occur in a non-linear fashion. Additionally, as shown in Fig. 3, the temperature within the sample is non-uniform. This could affect solute distribution, further modifying the dendrite growth velocities away from the well-established case of directional solidification.

3.5. Dendrite fragmentation

Dendrite fragmentation was observed during the experiment, as shown in Figs. 8a and b show just prior to, and immediately after fragmentation. This dendrite is located close to the sample centre and is a small, undeveloped primary arm (compared with the dendrite in Fig. 6). This dendrite was connected to the base with a very narrow root (see inset in Fig. 8a), where fragmentation occurred. As can be seen, after detachment, the fragment moved upwards due to buoyancy, as the α-Al primary dendrites are less dense than the Cu-enriched liquid.

There are a number of different mechanisms proposed in the literature to explain dendrite fragmentation, including re-melting induced by thermal fluctuations [55], pinch-off driven by coarsening/minimising interfacial curvature, or Gibbs-Thompson effect [56,57], and mechanical bending [58]. Here we investigate the likelihood of each of these potential mechanisms in turn for this fragmentation event.

Thermal fluctuation - in our case, the bottom furnace was cooling at a constant rate; hence this is a very unlikely cause as there were no significant fluctuations. Pinch-off driven by curvature minimisation — this is reported to require relatively long times [57]; however, the fragment here happens quickly, between two tomographic scans (~9 s). Hence we would hypothesis minimising the curvature is one of the driving forces, but that other factors are also trigging fragmentation. Flow induced bending — this seems unlikely as the sample was very small and strong flows are not expected, and indeed, after breaking off, the fragment floats straight upwards with little sideways motion, suggesting no convective flows, just buoyancy is operative. Here using the 3D data given by X-ray tomographic imaging, the buoyancy stress (σ_b) at the root can be directly calculated with:

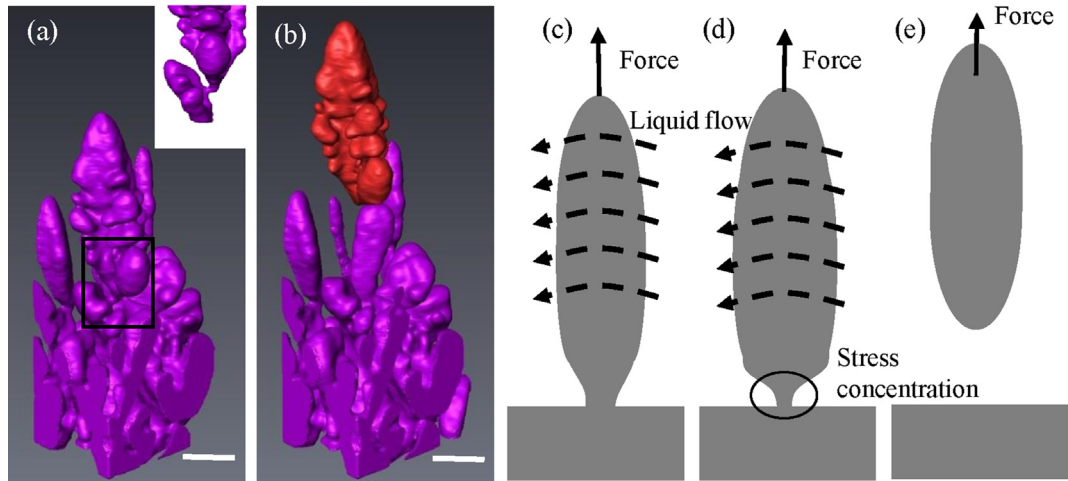**Fig. 7.** Time evolution of the dendrite tip velocity.

Fig. 8. Snapshot of dendrite fragmentation at (a) $t = 387$ s and (b) $t = 405$ s; (c), (d) and (e) schematic showing the breakage of dendrite due to liquation cracking (the scale bar in a and b is 100 μm).

$$\sigma_b = \frac{F_b}{s} = \frac{\rho_L V_f g}{s} \qquad (2)$$

where F_b is the buoyancy force, s is the cross-section area of the root (for this particular dendrite, its root has an equivalent radii of about 5.8 μm), ρ_L is the density of the liquid (2.54 g/cm^3 [59]), V_f is the volume of the fragmented solid, and g is the acceleration due to gravity. Based on the above calculation, σ_b was estimated in this experiment to be 1.8 kPa. The calculated value is 2 order of magnitude less than the bending stress (0.13 MPa) estimated by Billa et al. [60] for Al-0.73 wt%Cu alloy, and the yield stress (0.6 MPa) of Al at the melting point by Pilling and Hellawell [61]. Note that the stress responsible for dendrite fragmentation in the mushy zone is related to various factors, e.g. alloy composition, temperature, and solid fraction, hence it is not surprising that in different situations the stress would be significantly different.

We would propose that both buoyancy and curvature minimisation are the driving forces, but that these are either too small or slow to cause the fragmentation without additional mechanisms acting. Doherty et al. [58] hypothesised that dislocations form in the neck, recrystallizing to form high-angle grain boundaries. Again, this requires high stresses, whilst Karagadde et al. [39] recently proposed a mechanism termed *transgranular liquation cracking* (TLC), to explain the fragmentation of semi-solid globular grains at very low stresses. In TLC, the interdendritic liquid acts to accelerate the cracking, much like stress corrosion cracking, but initiating at dislocations formed under load, combined with a surface Rayleigh instability. We hypothesis that the stress localized in the dendrite root causes dislocation localization, and combined with the high curvature, significantly reduces the local melting temperature, and once initiated, the crack is accelerated [61].

In this case, although the stress induced on the dendrite root is very small, the surrounding Cu-enriched 'hot' liquid can easily penetrate into the solid phase in the region where dislocations were concentrated. The proposed mechanism for fragmentation is shown schematically in Fig. 8c–e. Coarsening reduced the root area of dendrite arm. The stress is probably induced by buoyancy, localized into the root of the dendrite, when assisted by liquidation, causing the dendrite to fragment. Similarly, Reinhart et al. [62] observed via X-ray radiography, secondary arms bent then fragmented during the growth of a columnar dendrite in an Al-7wt.%Si alloy, which was attributed to the stress concentrated at the arm

neck. This stress was caused by the gravity force as the solid phase is denser than the liquid [62]. Hence, it is believed that mechanical deformation from various sources (gravity [62], buoyancy, liquid flow, and external deformation [38,39]), when aligned with transgranular liquation cracking mechanisms, may play a much greater role in grain fragmentation during solidification than previous thought. Recent simulations of chemically assisted cracking show that the speed and energy required for cracking in other systems can be reduced by orders of magnitude [63].

3.6. Conclusions

This study reports the 4D (3D plus time) synchrotron tomographic quantification of columnar dendrite growth during directional solidification within a temperature gradient stage. Using power down mode cooling, the formation of cellular growth, the cellular-to-dendrite transition, together with the growth of established columnar dendrites were captured.

The imaging of the cellular growth showed much more complexity than in prior organic analogue and radiographic studies, where growth is constrained to effectively two dimensions between thin plates. Here, the cellular growth structures undulate both vertically and horizontally.

The onset of Mullins-Sekerka morphological instabilities were then quantified as the cellular front degenerated, with protrusions forming across the front as the first stage of the transition to dendritic growth. This transition was both rapid and relatively uniform across the whole front. Interestingly these protrusions formed both traditional dendrites and seaweed-like structures, with the latter being overgrowth.

Through competitive selection, the dendrites with favourable orientations aligned with the heat flow direction formed well-developed structures. The growth velocities of these structures were quantified.

Dendrite fragmentation was also observed and using the full 3D shapes, the potential mechanisms for fragmentation were qualitatively and quantitatively compared. For the fragmentation examined, it was hypothesised that a combination of stress induced by buoyancy and the Gibbs-Thomson effect are the two main driving forces, with the failure accelerated by a transgranular liquation cracking mechanism.

Data statement

A representative sample of research data from the experiments along with the plot data for the graphs in this manuscript is provided in supplementary material [http://dx.doi.org/10.1016/j.actamat.2016.07.002]. The underlying data is not provided online due to its very large size.

Acknowledgement

References

[1] W. Kurz, D.J. Fisher, Fundamentals of Solidification, 1986.

[2] J. Warren, Dendritic crystals: rule of thumb breaks down, Nat. Mater 5 (2006) 595–596, http://dx.doi.org/10.1038/nmat1702.

[3] T. Haxhimali, A. Karma, F. Gonzales, M. Rappaz, Orientation selection in dendritic evolution, Nat. Mater 5 (2006) 660–664, http://dx.doi.org/10.1038/nmat1693.

[4] J. Dantzig, M. Rappaz, Solidification: Methods, Microstructure and Modeling, EFPL Press, 2009.

[5] S. Tin, T. Pollock, Stabilization of thermosolutal convective instabilities in Ni-based single-crystal superalloys: carbide precipitation and rayleigh numbers, Metall. Mater. Trans. A 34 (2003) 20–22. http://link.springer.com/article/10.1007/s11661-003-0160-7 (accessed January 4, 2014).

[6] E. Ben-Jacob, P. Garik, The formation of patterns in non-equilibrium growth, Nature 343 (1990) 523–530, http://dx.doi.org/10.1038/343523a0.

[7] D.S. Eastwood, V. Yufit, J. Gelb, A. Gu, R.S. Bradley, S.J. Harris, et al., Lithiation-induced dilation mapping in a lithium-ion battery electrode by 3D X-ray microscopy and digital volume correlation, Adv. Energy Mater 4 (2014) 1–7, http://dx.doi.org/10.1002/aenm.201300506.

[8] V. Fleury, Branched fractal patterns in non-equilibrium electrochemical deposition from oscillatory nucleation and growth, Nature 390 (1997) 145–148, http://dx.doi.org/10.1038/36522.

[9] R. Trivedi, S. Liu, S. Williams, Interface pattern formation in nonlinear dissipative systems, Nat. Mater 1 (2002) 157–159, http://dx.doi.org/10.1038/nmat749.

[10] J. Nittmann, G. Daccord, H.E. Stanley, Fractal growth of viscous fingers: quantitative characterization of a fluid instability phenomenon, Nature 314 (1985) 141.

[11] W.W. Mullins, R.F. Sekerka, Stability of a planar interface during solidification of a dilute binary alloy, J. Appl. Phys. 35 (1964) 444–451, http://dx.doi.org/10.1063/1.1713333.

[12] A. Kao, P.D. Lee, K. Pericleous, Influence of a slow rotating magnetic field in thermoelectric magnetohydrodynamic processing of alloys, ISIJ Int. 54 (2014) 1283–1287.

[13] L. Yuan, P.D. Lee, A new mechanism for freckle initiation based on microstructural level simulation, Acta Mater 60 (2012) 4917–4926, http://dx.doi.org/10.1016/j.actamat.2012.04.043.

[14] M. Rappaz, Modeling and characterization of grain structures and defects in solidification, Curr. Opin. Solid State Mater. Sci. 20 (2016) 37–45, http://dx.doi.org/10.1016/j.cossms.2015.07.002.

[15] K. Jackson, J. Hunt, Transparent compounds that freeze like metals, Acta Metall. 13 (1965) 1212–1215.

[16] R. Trivedi, K. Somboonsuk, Patern formation during the directional solidification of binary systems, Acta Mater 33 (1985) 1061–1068.

[17] A. Bogno, H. Nguyen-Thi, A. Buffet, G. Reinhart, B. Billia, N. Mangelinck-Noël, et al., Analysis by synchrotron X-ray radiography of convection effects on the dynamic evolution of the solid–liquid interface and on solute distribution during the initial transient of solidification, Acta Mater 59 (2011) 4356–4365, http://dx.doi.org/10.1016/j.actamat.2011.03.059.

[18] N. Shevchenko, O. Roshchupkina, O. Sokolova, S. Eckert, The effect of natural and forced melt convection on dendritic solidification in Ga–In alloys, J. Cryst. Growth 417 (2015) 1–8, http://dx.doi.org/10.1016/j.jcrysgro.2014.11.043.

[19] A. Prasad, S.D. McDonald, H. Yasuda, K. Nogita, D.H. StJohn, A real-time synchrotron X-ray study of primary phase nucleation and formation in hypoeutectic Al-Si alloys, J. Cryst. Growth (2015), http://dx.doi.org/10.1016/j.jcrysgro.2015.06.024.

[20] A.J. Clarke, D. Tourret, S.D. Imhoff, P.J. Gibbs, K. Fezzaa, J.C. Cooley, et al., X-ray imaging and controlled solidification of Al-Cu alloys toward microstructures by design, Adv. Eng. Mater 17 (2015) 454–459, http://dx.doi.org/10.1002/adem.201400469.

[21] J.D. Hunt, K.A. Jackson, H. Brown, Temperature gradient microscope stage suitable for freezing materials with melting points between -100 and +200 degree C, Rev. Sci. Instrum. 37 (1966) 805, http://dx.doi.org/10.1063/1.1720336.

[22] P.D. Lee, J.D. Hunt, Hydrogen porosity in directional solidified aluminium-copper alloys:in situ observation, Acta Mater 45 (1997) 4155–4169, http://dx.doi.org/10.1016/S1359-6454(97)00081-5.

[23] G. Reinhart, A. Buffet, H. Nguyen-Thi, B. Billia, H. Jung, N. Mangelinck-Noël, et al., In-situ and real-time analysis of the formation of strains and microstructure defects during solidification of Al-3.5 Wt Pct Ni alloys, Metall. Mater. Trans. A 39 (2008) 865–874, http://dx.doi.org/10.1007/s11661-007-9449-2.

[24] W. Losert, B. Shi, H. Cummins, Evolution of dendritic patterns during alloy solidification: onset of the initial instability, Proc. Natl. Acad. Sci. U. S. A. 95 (1998) 431–438.

[25] M. Zhang, T. Maxworthy, The interactive dynamics of flow and directional solidification in a Hele-Shaw cell Part 1. Experimental investigation of parallel shear flow, J. Fluid Mech. 470 (2002) 247–268, http://dx.doi.org/10.1017/S0022112002002033.

[26] W. Losert, B.Q. Shi, H.Z. Cummins, Evolution of dendritic patterns during alloy solidification: from the initial instability to the steady state, Proc. Natl. Acad. Sci. U. S. A. 95 (1998) 439–442, http://dx.doi.org/10.1073/pnas.95.2.439.

[27] R.H. Mathiesen, L. Arnberg, X-ray radiography observations of columnar dendritic growth and constitutional undercooling in an Al–30wt%Cu alloy, Acta Mater 53 (2005) 947–956, http://dx.doi.org/10.1016/j.actamat.2004.10.050.

[28] L. Arnberg, R.H. Mathiesen, The real-time, high-resolution X-ray video microscopy of solidification in aluminum alloys, Jom 59 (2007) 20–26, http://dx.doi.org/10.1007/s11837-007-0099-z.

[29] E. Liotti, A. Lui, R. Vincent, S. Kumar, Z. Guo, T. Connolley, et al., A synchrotron X-ray radiography study of dendrite fragmentation induced by a pulsed electromagnetic field in an Al–15Cu alloy, Acta Mater 70 (2014) 228–239, http://dx.doi.org/10.1016/j.actamat.2014.02.024.

[30] R.H. Mathiesen, L. Arnberg, P. Bleuet, A. Somogyi, Crystal fragmentation and columnar-to-equiaxed transitions in Al-Cu studied by Synchrotron x-ray video microscopy, Metall. Mater. Trans. A Phys. Metall. Mater. Sci. 37 (2006) 2515–2524, http://dx.doi.org/10.1007/BF02586224.

[31] H. Yasuda, Y. Yamamoto, N. Nakatsuka, T. Nagira, M. Yoshiya, A. Sugiyama, et al., In situ observation of nucleation, fragmentation and microstructure evolution in Sn-Bi and Al-Cu alloys, Int. J. Cast. Met. Res. 21 (2008) 125–128, http://dx.doi.org/10.1179/136404608X361800.

[32] A. Bogno, H. Nguyen-Thi, G. Reinhart, B. Billia, J. Baruchel, Growth and interaction of dendritic equiaxed grains: in situ characterization by synchrotron X-ray radiography, Acta Mater 61 (2013) 1303–1315, http://dx.doi.org/10.1016/j.actamat.2012.11.008.

[33] J. Wang, Y. Fautrelle, Z.M. Ren, X. Li, H. Nguyen-Thi, N. Mangelinck-Noel, et al., Thermoelectric magnetic force acting on the solid during directional solidification under a static magnetic field, Appl. Phys. Lett. 101 (2012), http://dx.doi.org/10.1063/1.4772510.

[34] J.W. Gibbs, K.A. Mohan, E.B. Gulsoy, A.J. Shahani, X. Xiao, C.A. Bouman, et al., The three-dimensional morphology of growing dendrites, Sci. Rep. 5 (2015) 11824, http://dx.doi.org/10.1038/srep11824.

[35] O. Ludwig, M. Dimichiel, L.U.C. Salvo, P. Falus, In-situ three-dimensional microstructural investigation of solidification of an Al-Cu alloy by ultrafast X-ray microtomography, Metall. Mater. Trans. A 36 (2005) 1515–1523.

[36] R. Daudin, S. Terzi, P. Lhuissier, L. Salvo, E. Boller, Remelting and solidification of a 6082 Al alloy containing submicron yttria particles: 4D experimental study by in situ X-ray microtomography, Mater. Des. 87 (2015) 313–317, http://dx.doi.org/10.1016/j.matdes.2015.07.141.

[37] L.K. Aagesen, J.L. Fife, E.M. Lauridsen, P.W. Voorhees, The evolution of interfacial morphology during coarsening: a comparison between 4D experiments and phase-field simulations, Scr. Mater 64 (2011) 394–397, http://dx.doi.org/10.1016/j.scriptamat.2010.10.040.

[38] B. Cai, S. Karagadde, L. Yuan, T.J. Marrow, T. Connolley, P.D. Lee, In situ synchrotron tomographic quantification of granular and intragranular deformation during semi-solid compression of an equiaxed dendritic Al–Cu alloy, Acta Mater 76 (2014) 371–380, http://dx.doi.org/10.1016/j.actamat.2014.05.035.

[39] S. Karagadde, P.D. Lee, B. Cai, J.L. Fife, M.A. Azeem, K.M. Kareh, et al., Transgranular liquation cracking of grains in the semi-solid state, Nat. Commun. 6 (2015) 8300, http://dx.doi.org/10.1038/ncomms9300.

[40] K.M. Kareh, P.D. Lee, R.C. Atwood, T. Connolley, C.M. Gourlay, Revealing the micromechanisms behind semi-solid metal deformation with time-resolved X-ray tomography, Nat. Commun. 5 (2014) 4464, http://dx.doi.org/10.1038/ncomms5464.

[41] M. Drakopoulos, T. Connolley, C. Reinhard, R. Atwood, O. Magdysyuk, N. Vo, et al., I12: the joint engineering, environment and processing (JEEP) beamline at Diamond Light source, J. Synchrotron Radiat. 22 (2015) 1–10, http://dx.doi.org/10.1107/S1600577515003513.

[42] S. Titarenko, P.J. Withers, A. Yagola, An analytical formula for ring artefact suppression in X-ray tomography, Appl. Math. Lett. 23 (2010) 1489–1495, http://dx.doi.org/10.1016/j.aml.2010.08.022.

[43] N. Otsu, A threshold selection method from gray-level histograms, Syst. Man.

Cybern. IEEE Trans. 9 (1979) 62–66.

[44] M. Doube, M.M. Kłosowski, I. Arganda-Carreras, F.P. Cordelières, R.P. Dougherty, J.S. Jackson, et al., BoneJ: free and extensible bone image analysis in ImageJ, Bone 47 (2010) 1076–1079. http://www.sciencedirect.com/science/article/pii/S8756328210014419 (accessed December 17, 2013).

[45] G. Salloum Abou Jaoudé, G. Reinhart, H. Nguyen-Thi, H. Combeau, M. Založnik, T. Schenk, et al., In situ experimental observation of the time evolution of a dendritic mushy zone in a fixed temperature gradient, Comptes Rendus - Mec. 341 (2013) 421–428, http://dx.doi.org/10.1016/j.crme.2013.01.013.

[46] P.D. Lee, A. Chirazi, D. See, Modeling microporosity in aluminum–silicon alloys: a review, J. Light Met. 1 (2001) 15–30 (accessed December 14, 2013), http://www.sciencedirect.com/science/article/pii/S1471531700000031.

[47] L. Yuan, P.D. Lee, A new mechanism for freckle initiation based on microstructural level simulation, Acta Mater 60 (2012) 4917–4926, http://dx.doi.org/10.1016/j.actamat.2012.04.043.

[48] J.S. Langer, Instabilities and pattern formation in crystal growth, Rev. Mod. Phys. 52 (1980) 1–28, http://dx.doi.org/10.1103/RevModPhys.52.1.

[49] S. Akamatsu, G. Faivre, T. Ihle, Symmetry-broken double fingers and seaweed patterns in thin-film directional solidification of a nonfaceted cubic crystal, Phys. Rev. E 51 (1995) 4751–4773, http://dx.doi.org/10.1103/PhysRevE.51.4751.

[50] A. Pocheau, J. Deschamps, M. Georgelin, Dendrite growth directions and morphology in the directional solidification of anisotropic materials, Jom 59 (2007) 71–76, http://dx.doi.org/10.1007/s11837-007-0093-5.

[51] A.G. Borisov, O.P. Fedorov, V.V. Maslov, Growth of succinonitrile dendrites in different crystallographic directions, J. Cryst. Growth 112 (1991) 463–466, http://dx.doi.org/10.1016/0022-0248(91)90324-X.

[52] Y. Chen, B. Billia, D.Z. Li, H. Nguyen-Thi, N.M. Xiao, A.A. Bogno, Tip-splitting instability and transition to seaweed growth during alloy solidification in anisotropically preferred growth direction, Acta Mater 66 (2014) 219–231, http://dx.doi.org/10.1016/j.actamat.2013.11.069.

[53] Y. Shibuta, M. Ohno, T. Takaki, Solidification in a supercomputer: from crystal nuclei to dendrite assemblages, Jom 67 (2015) 1793–1804, http://dx.doi.org/10.1007/s11837-015-1452-2.

[54] S.C. Huang, M.E. Glicksman, Overview 12: fundamentals of dendritic solidification-II development of sidebranch structure, Acta Metall. 29 (1981) 717–734, http://dx.doi.org/10.1016/0001-6160(81)90116-4.

[55] A. Hellawell, S. Liu, S.Z. Lu, Dendrite fragmentation and the effects of fluid flow in castings, J. Mater 49 (1997) 18–20, http://dx.doi.org/10.1007/BF02914650.

[56] H. Neumann-Heyme, K. Eckert, C. Beckermann, Dendrite fragmentation in alloy solidification due to sidearm pinch-off, Phys. Rev. E - Stat. Nonlinear, Soft Matter Phys. 92 (2015) 1–5, http://dx.doi.org/10.1103/PhysRevE.92.060401.

[57] L.K. Aagesen, A.E. Johnson, J.L. Fife, P.W. Voorhees, M.J. Miksis, S.O. Poulsen, et al., Universality and self-similarity in pinch-off of rods by bulk diffusion, Nat. Phys. 6 (2010) 796–800, http://dx.doi.org/10.1038/nphys1737.

[58] R.D. Doherty, H.-I. Lee, E.A. Feest, Microstructure of stir-cast metals, Mater. Sci. Eng. 65 (1984) 181–189, http://dx.doi.org/10.1016/0025-5416(84)90211-8.

[59] Y. Plevachuk, V. Sklyarchuk, A. Yakymovych, S. Eckert, B. Willers, K. Eigenfeld, Density, viscosity, and electrical conductivity of hypoeutectic Al-Cu liquid alloys, Metall. Mater. Trans. A Phys. Metall. Mater. Sci. 39 (2008) 3040–3045, http://dx.doi.org/10.1007/s11661-008-9659-2.

[60] B. Billia, N. Bergeon, H.N. Thi, H. Jamgotchian, J. Gastaldi, G. Grange, Cumulative mechanical moments and microstructure deformation induced by growth shape in columnar solidification, Phys. Rev. Lett. 93 (2004) 1–4, http://dx.doi.org/10.1103/PhysRevLett.93.126105.

[61] J. Pilling, A. Hellawell, Mechanical deformation of dendrites by fluid flow, Metall. Mater. Trans. A 27 (1996) 229–232, http://dx.doi.org/10.1007/BF02647763.

[62] G. Reinhart, H. Nguyen-Thi, N. Mangelinck-Noël, J. Baruchel, B. Billia, Situ investigation of dendrite deformation during upward solidification of Al-7wt.%Si, Jom 66 (2014) 1408–1414, http://dx.doi.org/10.1007/s11837-014-1030-z.

[63] A. Gleizer, G. Peralta, J.R. Kermode, A. De Vita, D. Sherman, Dissociative chemisorption of O2 inducing stress corrosion cracking in silicon crystals, Phys. Rev. Lett. 112 (2014) 1–5, http://dx.doi.org/10.1103/PhysRevLett.112.115501.